(12)

USAFA-TN-83-7

AD-A132 182

Department of Aeronautics
Dean of the Faculty
United States Air Force Academy
Colorado 80840

WAKE CHARACTERISTICS AND INTERACTIONS OF THE CANARD/WING LIFTING SURFACE CONFIGURATION OF THE X-29 FORWARD-SWEPT WING FLIGHT DEMONSTRATOR

Final

TECHNICAL NOTE
USAFA-TN-83-7

Griffin, K.E.

Haerter, E.C.

Smith, B.R.

15 AUGUST 1983

Any views expressed in this paper are those of the author. They should not be interpreted as reflecting the views of the USAF Academy or the official opinion of any governmental agency. Notes are not reviewed for content or quality by the USAF Academy but are published primarily as a service to the faculty to facilitate internal research communication.

This Technical Note has been cleared for open publication and/or public release by the appropriate Office of Information in accordance with AFR 190-17 and DODD 5230.9. There is no objection to unlimited distribution of this Technical Note to the public at large or by DDC to the National Technical Information Service.

This Technical Note is approved for publication.

THOMAS E. McCANN, Lt Colonel, USAF
Director of Research, Studies, and Analysis

Forward

This technical note is the final report on a series of tests of forward-swept wing and canard wake interactions. The tests in this document were conducted at the Aeronautics Laboratory of the USAF Academy during the period 1 January 1983 to 29 July 1983. This technical effort was sponsored by the Defense Advanced Research Projects Agency (DARPA) and administered as ARPA 4364 by Colonel James Allburn. Captain K.E. Griffin, the principal investigator, was assisted by the staff and cadets at the USAF Academy.

This report documents the location of the canard wake and its interactions with the upper-surface flow field of the forward-swept wing of the X-29. The flow field of a 1/10-scale model of the X-29 is surveyed with the canard at different angles of attack and with the canard removed. Comparing these configurations by means of velocity and pressure plots revealed the effects of the canard on the wing. The detailed pressure and velocity data is stored on a 9-track magnetic tape at the Aeronautics Laboratory, where it is available to any interested investigator.

WAKE CHARACTERISTICS AND INTERACTIONS OF THE CANARD/WING LIFTING SURFACE CONFIGURATION OF THE X-29 FORWARD-SWEPT WING FLIGHT DEMONSTRATOR

E.C. Haerter*, B.R. Smith*, and K.E. Griffin**

Abstract

This technical note summarizes experimental lifting-surface wake data taken from a 1/10-scale, reflection-plane model of the X-29 Forward-Swept Wing Demonstrator. The model is configured with and without the canard to illustrate the canard/wing wake interactions. The data collected comprises total, dynamic, and static pressures as well as local velocity magnitudes and directions for a series of points around this model. The data points are arrayed to include flow regions near the model as well as the freestream wake regions downstream of its canard and wing.

I. Introduction

Placing lifting surfaces, such as canards, upstream from the primary lifting surface introduces new flow-field uncertainties. These surfaces produce aircraft trimming loads that introduce trimming surface/primary wing flow-field interactions that are not found in conventional aft-tail configurations. The 1/10-scale, reflection-plane model, shown in Figure 1, is used in this test effort to examine the major pressure and velocity field effects of the interaction between the wake from the canard and the flow field of the forward-swept wing. The configuration is modeled from the X-29 Forward-Swept Wing Demonstrator Aircraft. The measurement of freestream values of total, static, and dynamic pressure and of the local velocity vector in the complex flow fields aft of lifting surfaces is made possible by a seven-hole pressure probe and data acquisition system. This system was developed at the Aeronautics Laboratory at the USAF Academy for

*Cadet, USAF Academy
**Captain, USAF Academy, Assistant Professor of Aeronautics, DFAN

the purpose of surveying unknown flow fields. Sample data, along with some interpretation, is presented to illustrate the flow interactions at selected locations along the model. This effort culminates a three-part investigation into lifting-surface wakes. Part one examined a simple, generic forward-swept wing configuration, as is documented in USAFA-TN-82-4 (Ref. 1). The second part examined two simple lifting-surface planforms used in the past to study wake characteristics: a low aspect-ratio delta and a low aspect-ratio flapped plate. These tests are documented in USAFA-TN-83-6 (Ref. 2).

Different canard angles were tested to observe their effects on the wake interactions. The data summarizing these effects is presented here in graphical form, showing velocity and pressure values. The progression downstream of the interactions is suggested by the plots of the lifting-surface wake regions at successive downstream locations.

II. Background

The presence of lifting surfaces or bodies in otherwise uniform flow causes changes in total pressure that are carried downstream as well as velocity changes that result in downwash. These total pressure changes are caused by irreversible changes in the energy of the flow due to viscous losses. These viscous losses occur in all boundary layers as well as near the core of vortex systems and are caused by large velocity gradients. The

loss in total pressure is apparent in these regions when measurements of total pressure are made with a pitot probe. The calibration of a pitot probe assumes the total reversible recovery of the dynamic pressure at the pressure port. The irreversible energy changes due to viscous effects just mentioned do not allow this fully reversible pressure recovery at the pitot port. The downstream location of the wakes of wings or bodies as well as the vortex systems that they generate can be obtained, then, by observing the loss in total pressure occuring in the streamlines that have passed near them.

This loss in total pressure, which is discernible in the flow for some distance downstream, is measured in this test effort with the seven-hole pressure probe. The velocity fields downstream of lifting surfaces and bodies are highly complex, with widely varying velocity vectors that usually cannot be predicted. Given this unpredictability, a single-port pitot probe cannot be used to measure total pressure, since the velocity vector must be known beforehand at all data point locations in order to properly orient the probe to measure total pressure. The seven-hole pressure probe is not limited in this way.

The seven-hole pressure probe, developed at the Aeronautics Laboratory of the USAF Academy under sponsorship of the NASA Ames Research Center (Ref. 3), is shown in Figure 2. Six pressure ports are equally spaced on the conical face of the probe around the seventh port, which is located at probe centerline. Using these seven pressure ports and a series of calibration equations,

the total, static, and dynamic pressures as well as the local flow velocity vector can be obtained for any data point location in the flow field where the probe can be positioned. The velocity vector can be as much as 80 degrees off-angle with respect to the seven-hole probe centerline without affecting the accuracy of its measurements (Ref. 4). Therefore, even the complex and unpredictable flow fields downstream from canard/wing combinations can be safely surveyed without concern that the probe is too greatly misaligned with the flow. The probe in use at present has been calibrated to measure flow velocities up to Mach 2, but the local flow velocities for the low-speed tests documented here rarely exceed Mach .5. The ability to extract these pressures and velocities from the seven-hole probe lies in the high-speed digital minicomputer contained in the probe data acquisition system. Seven sets of fourth-order simultaneous equations, defined for seven possible flow angle regions, convert the raw pressure values at the seven ports to the total, static, and dynamic values on a real time basis during testing. The coefficients in these equations are defined in calibration tests using known flow conditions and probe orientations. This real time data reduction permits data plotting during the tests to avoid missing unexpected flow characteristics or characteristics in unexpected locations.

III. Experimental Apparatus

A. Wind Tunnel

Tests were conducted in the subsonic continuous-flow wind tunnel at the Aeronautics Laboratory shown in Figure 3. It has a 2-foot by 3-foot test section that is 70 inches long, permitting the use of the 1/10-scale, reflection-plane X-29 model. Density, temperature, and pressure in the wind tunnel are prescribed by local atmospheric conditions. Speeds are available from 50 to 400 feet per second providing Reynolds numbers in the range of .2 x 10 to 1.6 x 10 per foot. The flow speed used for this test is 150 feet per second.

B. Model

The model used for these tests is the 1/10-scale, reflection-plane representation of the X-29 shown in Figure 1. It is constructed of steel- and fiberglass-reinforced epoxy. The inlets are vented to the tail cone. The model is mounted in the wind tunnel (with the wings horizontal) by means of a vertical splitter plate, which minimizes the wind tunnel boundary layer effects near the model body. Two wing configurations are possible: a low-speed, high-lift flap configuration (used for these tests) and a high-speed, high-lift flap configuration (that will be tested in the future). The canard has unlimited angle travel, with its angle of attack measured in relation to the aircraft centerline (which is also the engine thrust line). The canard is also removable to allow wing-only flow field comparisons. The model angle-of-attack range is between plus and minus 20 degrees with respect to the wind-tunnel centerline. The

model angle used for all of the data presented here is 6 degrees. This model angle permits smooth and attached flow over the wing (without the canard) while avoiding any separation effects about either the leading or trailing edge.

C. Seven-Hole Probe System

The seven-hole probe and positioning hardware are shown in Figure 2. Each pressure port at the probe tip is connected by flexible tubing to electronic pressure transducers just outside the wind tunnel. These transducers create an electrical analog signal of the port pressures for input to a digital computer. The dwell time of the probe at each data point location is such that all pressure transients have been damped out before recording the port pressures.

A PDP 11/45 digital computer is used to convert the raw port pressures to readily usable data. The computer reads these port pressures directly through an analog-to-digital converter. The digitized port pressures are then converted (on a real-time basis) to total, static, and dynamic pressures and velocity vectors by means of predetermined calibration equations stored in the computer. The data is then stored on a magnetic disk for quick retrieval. After the pressure port data is recorded at a preselected geometric location, the computer directs the mechanical traverse to position the probe at the next data point location. These geometric data point locations are pre-selected and stored in the computer in groups of 100, organized in

trapezoidal grid patterns. Opportunities to plot the accumulating data during a test sequence are available periodically to refine the grid work of data points.

IV. Results

The test results are highlighted and summarized here in a series of plots depicting the cross velocities and total pressures using 5 sets of data points. These sets are organized within 5 planes that have constant streamwise locations within the wind tunnel. The streamwise locations of these planes relative to the model are illustrated in Figure 4. All data planes are oriented so that their unit normals are parallel to the test section's centerline. Data Plane 1 is .2 inches downstream from the crank in the canard's trailing edge. Plane 2 intersects the leading-edge crank of the forward-swept wing. Plane 4 is .4 inches downstream from the exposed wing root trailing edge. Plane 3 is half way between Plane 2 and Plane 4 streamwise. Plane 5 is .2 inches downstream from the strake trailing edge. In each of these planes a series of data points is placed so that the upper-surface flow field or the freestream wake of the canard and/or wing can be adequately defined using measurements taken at these points. The data point locations are also chosen so that the probe positioning system can locate the probe at each point without striking the model.

The cross-velocity vectors and the contour lines of constant loss in total pressure are plotted for each plane. This

combination of velocity and total pressure loss provides the best graphical display of the flow field and wake characteristics. The data planes are ordered according to streamwise location, with the most upstream location presented first. A sense of the movement and development of the wake characteristics from a lifting surface can be gained by comparing figures as they represent progressively more downstream locations.

The velocity field in and around a lifting surface is the easiest form of flow-field data to visualize. Therefore, the velocity patterns are most useful in interpreting the results of these wake surveys. In this data the velocity patterns are depicted by means of cross-velocity vectors representing the cross flow and downwash at each of the data point locations. The length of the vectors indicates relative magnitude; their tail defines the geometric location of the data points; and the arrowhead indicates the positive flow directions. The component plotted in these cross-velocity figures is the component of the total velocity vector that lies in the plane of data points. The downwash is thus defined in terms of the freestream flow direction or wind tunnel centerline rather than a coordinate system attached to the model. Streamwise vorticity appears as localized rotary motion, downwash appears as uniform downward motion, and lifting surface wakes appear as discontinuities in the vector directions of the downwash.

To complement the plots of cross-velocity vectors, contours of constant values of total-pressure loss are also plotted. Total

pressure losses are recorded here in non-dimensionalized form for ease in plotting. The total pressure coefficient, C_{P_o}, is defined so that, as the local total pressure at a particular data point, $P_{o_{Local}}$, drops below that of the freestream value, $P_{o_{Tunnel}}$, the coefficient C_{P_o} becomes negative.

$$C_{P_o} = \frac{P_{o_{Local}} - P_{o_{Tunnel}}}{P_{o_{Tunnel}} - P_{\infty_{Tunnel}}} \qquad (1)$$

This pressure difference is non-dimensionalized by the tunnel dynamic pressure. Using the same data point locations found in the velocity plots, contours of C_{P_o} define wake locations and vortex concentrations. For this paper a C_{P_o} range of 0 to -.4 is used for the pressure plots. In and around the vortex cores and the midplane of the strongest regions of the wakes, the loss in this total pressure coefficient can be much larger than -.4. However, to observe the more subtle wake signatures in the size of plots used in this report, only this narrow range in C_{P_o} is plotted.

To help the reader interprete data presented later, a plot of the cross velocity vectors of Data Plane 4 (as they would be seen relative to the wind tunnel model) has been constructed and is shown in Figure 5. The velocity plot is mounted on a glass plate that occupies the spatial location (relative to the model) of the data points of Data Plane 4. The wind tunnel model is viewed from the port side as mounted in the test section. The coordinate system used in all the data plots has its origin at the lower corner of the port side of the test section, which is the

near lower corner of the plane as seen in Figure 5. The x-coordinate is horizontal and positive, moving port to starboard relative to the model. The y-axis is vertical and in the positive lift direction relative to the model. The figure shows a perspective view of the data plane. A second view of this cross velocity plot from that plane is shown in Figure 6. This is a streamwise view of the same plane, showing the velocity field downstream of the lifting surfaces that created it. The view in Figure 6 is upstream towards the model, showing its port wing and canard upstream of the data plane. The association can be seen in this figure between the lifting surface tips and the downstream flow rotation from their tip vorticity.

A. Wing Only

In order to observe the effects of the canard wake on the flow field and wake of the wing upper surface, the velocity and pressure characteristics of the wing flow field with the canard removed are needed for comparison. In Figures 7 and 8 these characteristics are plotted for Data Planes 2 through 5. Figure 7 presents the cross-velocity vectors, and Figure 8 shows the pressure contours.

Four velocity plots are shown in Figure 7. Data Plane 2 (at the top) occupies the most upstream location, while the plots below (when viewed in sequence) show the flow field developement streamwise. Again, the view is upstream with the wing tip lying on the left of the plot and the fuselage on the right. Positive

lift is upwards in the y direction. The velocity vectors show both the wing tip vortex and the interior downwash that contains the wake. The discontinuity in this downwash field indicates the wake direction.

Figure 8 contains the total pressure contours corresponding to the data points and conditions illustrated in Figure 7. If the pressure coefficient range of .0 to -.4 is used, several wake characteristics can be seen. The tip vortex is shown at the left of each plot, and the wing wake is visible as the band of total pressure loss. Since the wing intersects significant parts of Data Planes 2 and 3, the upper-surface boundary layer is visible where the probe can come sufficiently close to the upper surface. The large disturbance in these boundary layers caused by the leading edge crank can be seen at approximately 19 inches on the x-axis. The crank disturbance can also be seen in the velocity plot of Data Plane 2 (Figure 7). Note the spanwise change in the flow direction at the crank location.

Keeping in mind the plots of the wing flow field without the canard (Figures 7 and 8), consider the flow fields in Figures 9 through 18. In these figures, the canard is in place and its position is varied from -20 to +20 degrees angle of attack. These plots are organized by data plane. Figures 9 and 10 are the velocity and pressure plots for Data Plane 1, Figures 11 and 12 are the same for Data Plane 2, etc. In each figure the 4 plots are taken from a single set of data points with the canard set at 20, 10, 0, and -20 degrees, respectively. The effect of canard

angle can be seen by comparing the plots to each other and to Figures 7 and 8.

B. Data Plane 1

The dominant features of Data Plane 1 (Figure 9) are due to the canard, since the wing is downstream of this location. Beginning at the -20 degree canard angle (the lowest plot in the figure), a well-defined tip vortex and upwash (negative downwash) appears. In reality, the canard is flying at only -14 degrees angle of attack, since the body is at +6 degrees with respect to the freestream. At the next plot up in the figure, 0 degrees, the canard is flying at a 6 degree absolute angle of attack, and the direction of the tip vortex rotation corresponds to a positive lift condition on the canard. Note that the downwash from the canard at this angle is strongly affected by the upwash that precedes the wing leading edge. The entire canard downwash is much stronger in the next plot above (the 10 degree canard angle). The flow field is still well defined. However, the plot of the flow field with the canard at 20 degrees shows irregular or ill-defined flow near the canard wake location. At this angle, the canard is producing a totally separated upper-surface flow field. This separated region is easily seen in the irregular vector directions inboard of the canard tip region. The strong downwash field above this region, extending to the region just outboard the canard tip, is curious. Since the extremely low pressure region on the canard's upper surface has been lost, the

strong pressure recovery at the canard tip is not there to create a strong, well-defined, canard-tip vortex. In addition, the flow conditions for all the data planes near the fuselage are strongly influenced by flow separation caused by the large inlets just upstream of the canard.

The total pressure contours in Figure 10 display lines representing constant values of C_{P_o}. The rings corresponding to the tip vortex encircle the canard-tip vortex core. Near the core, very large negative values of C_{P_o} (on the order of -6 in some cases) are measured. Therefore, these core values are outside the range used for plotting in Figure 10, and a blank space appears at the vortex core. In the plot for the 0 degree canard angle, the canard wake is clearly defined. The wake at the larger positive canard angles is not visible because the wing prevents the the probe from being positioned in these lower regions. Note that as the angle of the canard is increased to 10 degrees, the region of large C_{P_o} losses increases. This tip vortex is stronger due to the large canard angle of attack.

C. Data Plane 2

The velocity vectors and pressure contours for Data Plane 2 appear in Figures 11 and 12, respectively. The wing tip is upstream of this data plane, and the wing/plane intersection contains nearly the complete wing semi-span. Therefore, only the wing-tip vortex can be seen at this location. The wing wake begins at the more downstream wing trailing edge. This wing-tip

vortex does not change its core location when the canard angle is changed. The canard influence on the wing flow field becomes significant just outboard of the canard-tip vortex. The canard-tip vortex location is influenced by the wing and moves upward with the streamlines that follow the wing upper surface. Note that the spanwise location of the canard-tip vortex moves inboard as the absolute value of the canard angle increases. The downwash inboard of the wing-tip vortex must also change to upwash just outboard of the canard-tip vortex. Even though the canard-tip vortex moves inboard with canard angle increases, this wash transition appears at the same spanwise location. Finally, note the large differences in the upper surface wash on the wing with the canard at positive angles when compared to this data plane with no canard present. This large influence towards downwash illustrates the separation delay available for forward sweep when a canard trimming surface is used.

The pressure contours for Data Plane 2 (Figure 12) show the canard wake moving closer to the wing upper surface with increased canard angle of attack. The wing tip vortex is also shown. The boundary layer on the wing upper surface is visible with positive canard angles. The large disturbance near the fuselage moves vertically; with the canard angle at -20 degrees, it is barely visible at the wing root.

D. Data Plane 3

Downstream at Data Plane 3 (Figures 13 and 14) a

significant portion of the wing wake can be observed outboard of the canard-tip vortex. The velocity plots in Figure 13 show the strong wing-tip vortex maintaining its position and containing a well-defined, rotation-velocity profile that appears to be independent of the canard angle of attack. The canard-tip vortex, however, shows considerable degeneration when the canard is at 20 degrees angle of attack. With the canard at 10 degrees or less, a strong interaction appears between the inboard spanwise flow (at the immediate upper surface of the deployed trailing-edge flap of the wing) and the rotational flow of the canard-tip vortex. This interaction creates an S pattern, which is most evident in the plot for the 10 degrees canard angle. Note also the strong inboard flow component in the wing upper-surface flow downstream of the canard when the canard is at negative angles of attack. The discontinuity in the spanwise flow component of the wing downwash can now be used to define the wing wake location.

The pressure contours of Data Plane 3 (Figure 14) confirm the locations of the wake characteristics. The plot for the 20 degree canard angle also verifies the degeneration of the canard-tip vortex. The disturbance in pressure is now an amalgam of wing boundary layer, canard wake, and tip vortex without sharp definition of each characteristic. Note also that the location and strength of the wing wake seem relatively unaffected by different canard angles.

E. Data Plane 4

Figure 15 shows the velocity plots for Data Plane 4. This is the most upstream location containing all of the wing wake, and it does not intersect the wing itself. As in all the plots, the wing-tip vortex is well defined and remains in the same x,y location. The canard-tip vortex, however, is well defined only at the 0 and -20 degrees canard angles. At 20 degrees canard angle of attack, the rotary flow of a canard-tip vortex is not really defined. There are changes in the wing downwash downstream of the canard, but vortex flow has disappeared.

The effect of the canard wake on the spanwise component of the wing flow field can be seen at the 0 and 10 degree canard angles. A natural "wing fence" effect is formed just outboard of the canard-tip vortex. At this span location, the cross-velocity vectors lose their spanwise component. Inboard of this location, spanwise flow is outboard; conversely, outboard of this location, the spanwise flow is inboard. The wing wake can also be seen in the discontinuity in the downwash vectors. This is especially noticeable at the -20 degree canard angle.

The pressure contours of Data Plane 4 are plotted in Figure 16. The wing-tip vortex remains in the same location, but the wing wake begins to drift downward with the downwash. The canard wake can be identified just above the wing wake for the 0 degree canard angle, but for the larger canard angles the wing wake and canard wake pressure disturbances cannot be separated.

F. Data Plane 5

The velocity plots for Data Plane 5 are shown in Figure 17. The wing-tip vortex is still well defined and unaffected by the canard. Its vertical and horizontal positions remain fixed. The canard-tip vortex velocity signature for the 10 degree canard angle is faint at this streamwise location, while for the 0 degree canard angle, it is still well defined. The downwash influence from even the 20 degree canard angle is very strong; however, at this streamwise location the velocity discontinuity of the wing wake is not discernable, and the pressure contours must be used to find the wing wakes.

The pressure contours for this data plane are found in Figure 18. Although the wing wake signatures are becoming very weak, the pressure signatures of the canard tip, even for the 20 degree canard angle, remain very strong. Note how far down the wing wake has drifted in the presence of the wing downwash. This downward drift does not appear to be influenced by the presence of the canard.

V. Conclusion

Vortex systems for both the canard and the wing tips can be easily identified using the velocity and pressure plots. It appears that unless a tip-vortex core passes near another lifting surface, its location remains constant downstream of the generating lifting surface. The lifting-surface wake does drift with the downwash and appears to "unwrap" around the vortex core, but the core itself does not move.

The wake locations can best be identified by their pressure signatures. The relative strengths of the wakes are discernable, and locating parallel wakes in close proximity has been proved possible. In all the tests at the 6 degree aircraft angle of attack, no canard angle could be found that moved the canard wake below the wing.

The strong downwash influence of the canard on the inboard portion of the wing can be seen easily. It appears, however, that the upwash outboard of the canard (when it is at positive angles of attack) does not influence the outboard wing flow field significantly. The downward movement of the outboard wing wake, at progressively downstream locations, does not seem to be affected by the canard.

The vortex system created by the canard at large angles of attack (where significant canard flow separation exists) breaks down more quickly when moving downstream than does the vorticity created when the canard is at low angles of attack. The breakdown occurs from the inside out rather than the reverse. Perhaps the stronger vortex bursts much sooner than the weaker ones. This seems to be visible at the 20 degree canard angle of attack. Here the inner velocity vectors of the canard vortex become random, while the outer areas retain their rotary directions. This interior is thus a random, unsteady flow region that could be identified as the interior of a burst vortex. It remained stationary and well defined in all downstream data planes. This phenomenon could not be identified in the wing-tip vortex.

Future investigations should attempt to identify the bursting characteristic of these vortices, and its possible implications for the wing flow field. The high-speed wing should also be examined, since its smooth upper-surface contours should provide a configuration that would allow higher aircraft angles of attack before significant flow separation occurs. These higher angles of attack would change the geometric relationships of the canard wake and wing upper surface, allowing more separation.

References

1. Griffin, K.E., "Measurement of Wake Interactions of a Canard and Forward-Swept Wing," USAFA-TN-82-4, USAF Academy, July, 1982.

2. Kedzie, C.R. and Griffin, K.E., "Experimental Measurements of Wake Characteristics of Low Aspect-Ratio Delta and Flapped Plate Planforms," USAFA-TN-83-6, USAFA Academy, March, 1983.

3. Crandall, R. and Sisson, G., "Canard Wake Measurement and Description," Aeronautics Digest, USAFA-TR-81-4, USAF Academy, May, 1981.

4. Gerner, A. and Sisson, G., "Seven-Hole Probe Data Acquisition System," USAFA-TN-81-8, November, 1981.

Figure 1. Reflection-Plane Wind Tunnel Model in 1/10 Scale of the X-29

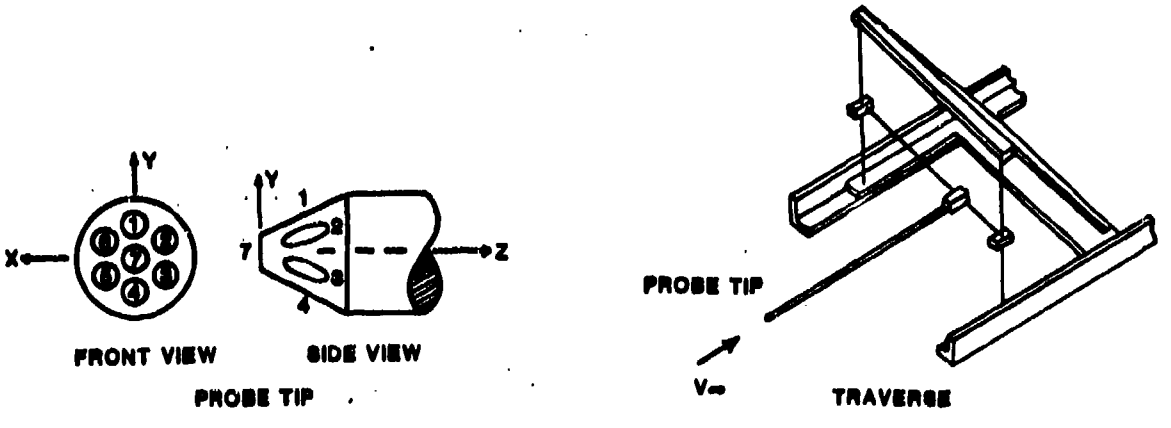

Figure 2. Seven-Hole Pressure Probe and Traverse

Figure 3. USAFA Subsonic Wind Tunnel

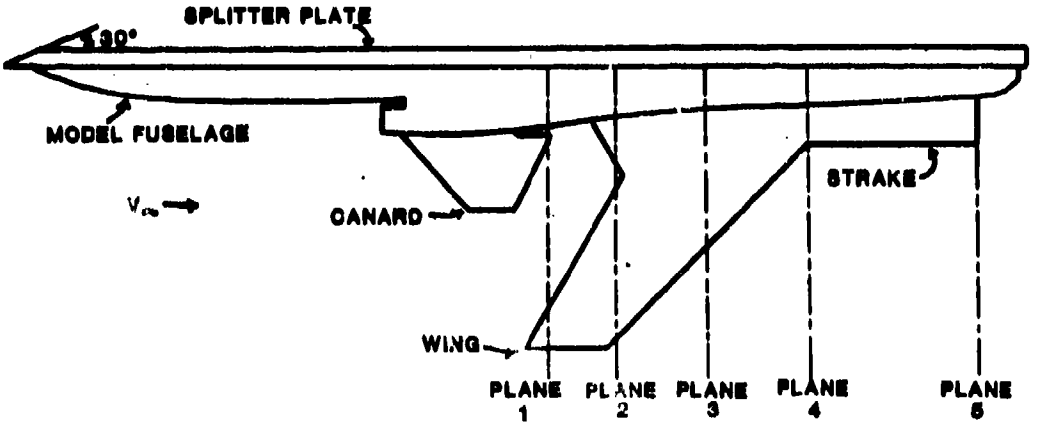

Figure 4. Data Planes' Geometric Location Relative to the X-29 Model Looking Down from the Top of the Test Section

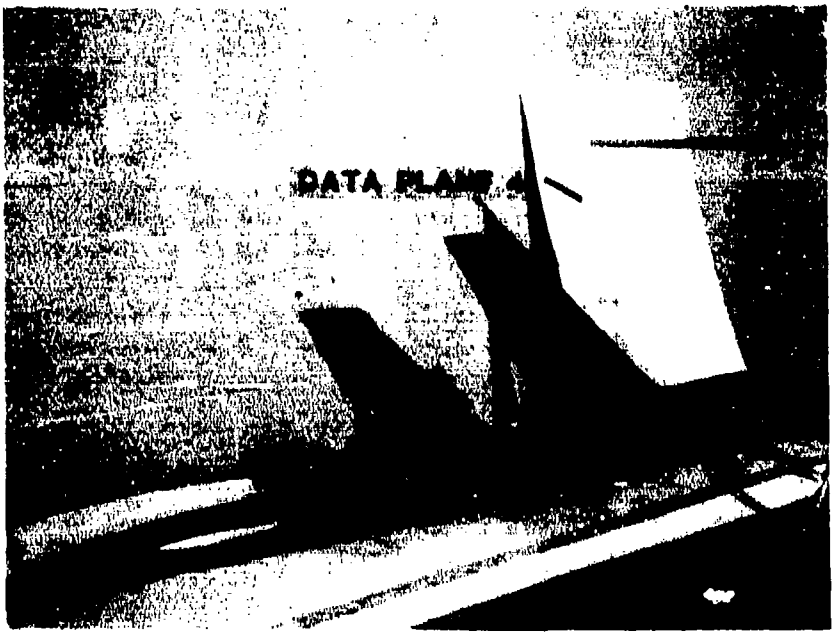

Figure 5. Pictorial Explanation of Data Plane 4

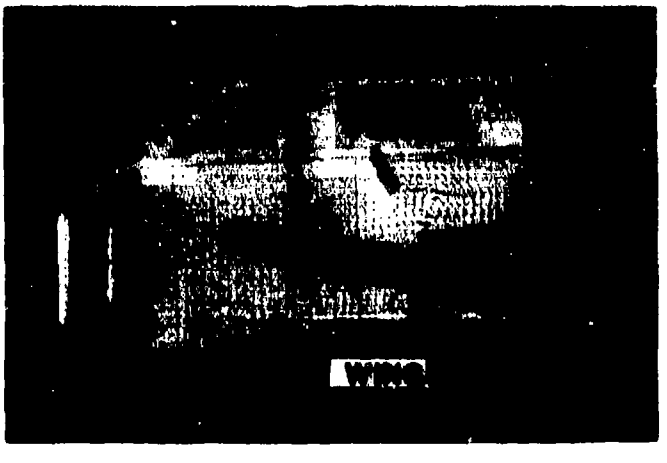

Figure 6. Cross Velocity Vectors for Points of Data Plane Looking Downstream in Test Section

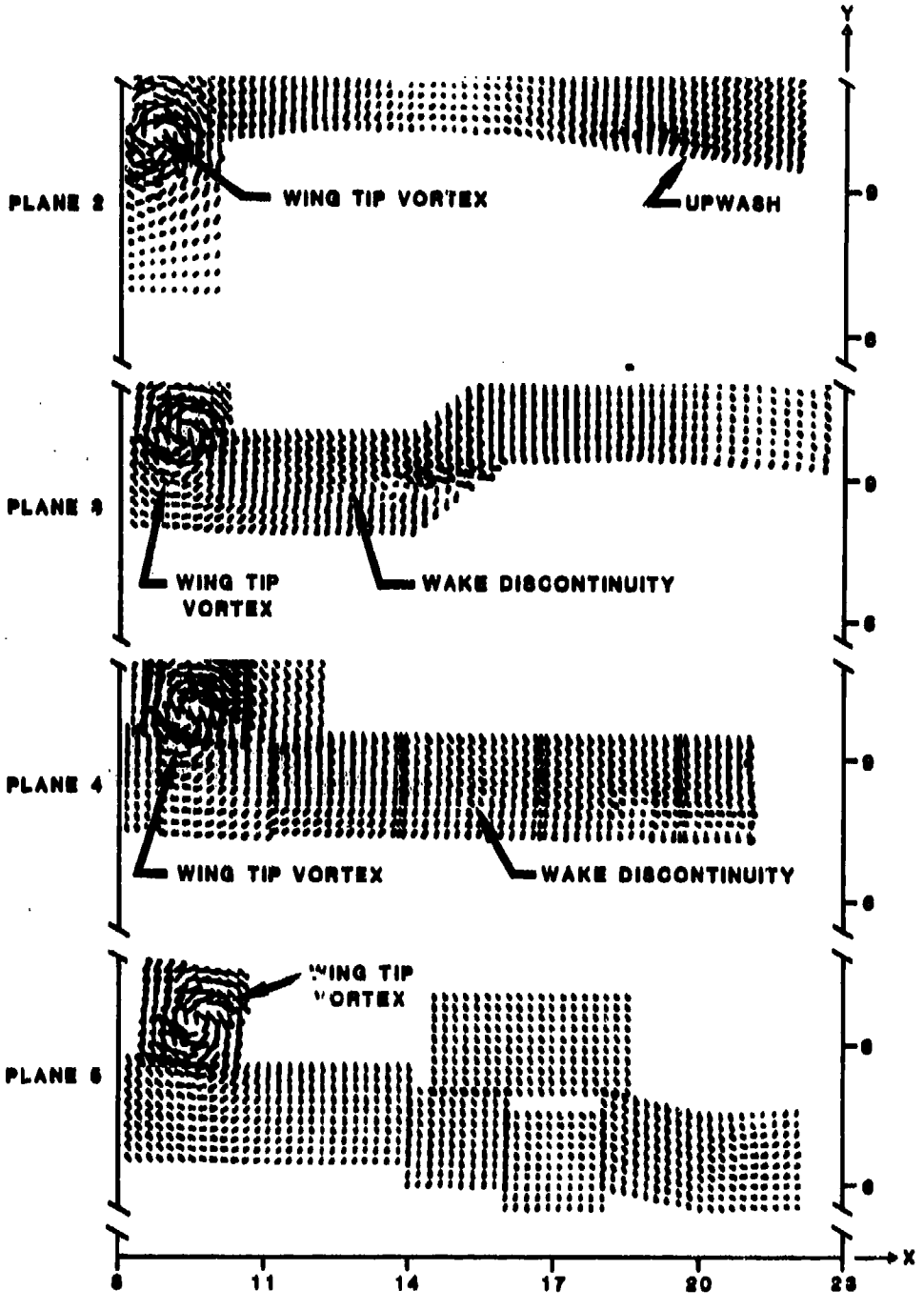

Figure 7. Cross-Velocity Vectors at Data Planes 2 through 4 with the Canard Removed

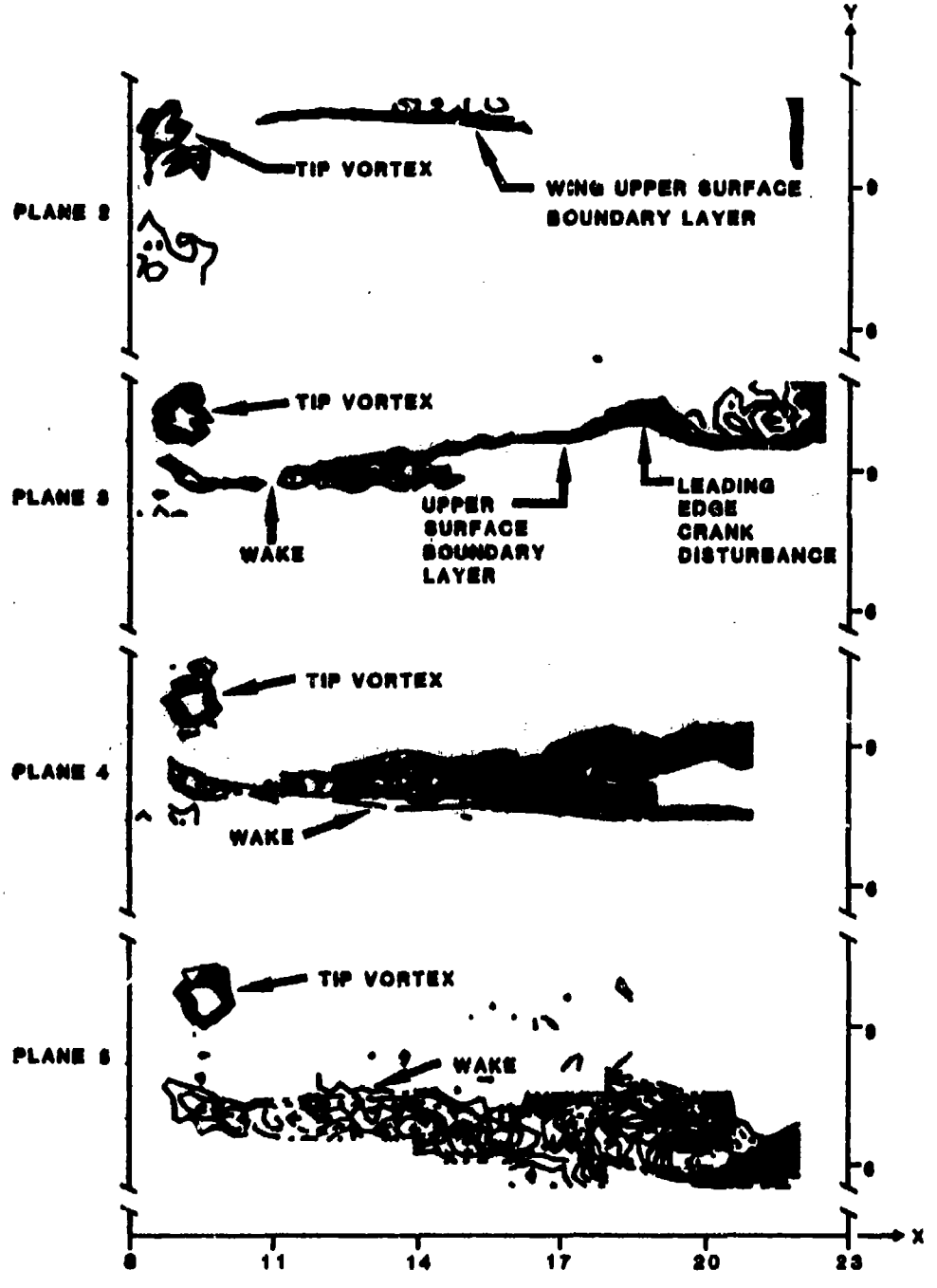

Figure 8. C_{P_o} Contour Plots for Data Planes 2 through 5 with the Canard Removed

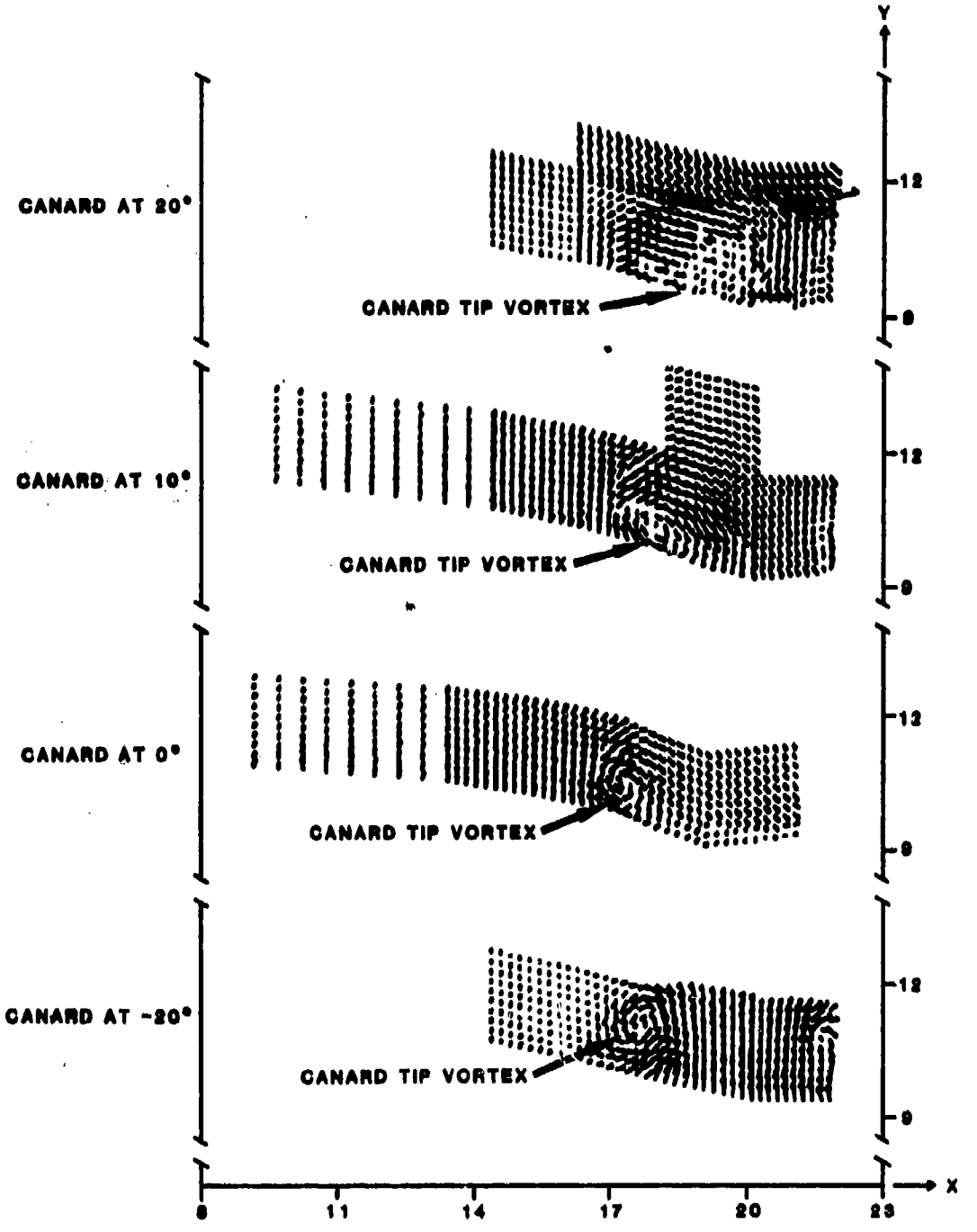

Figure 9. Velocity Vectors for Data Plane 1

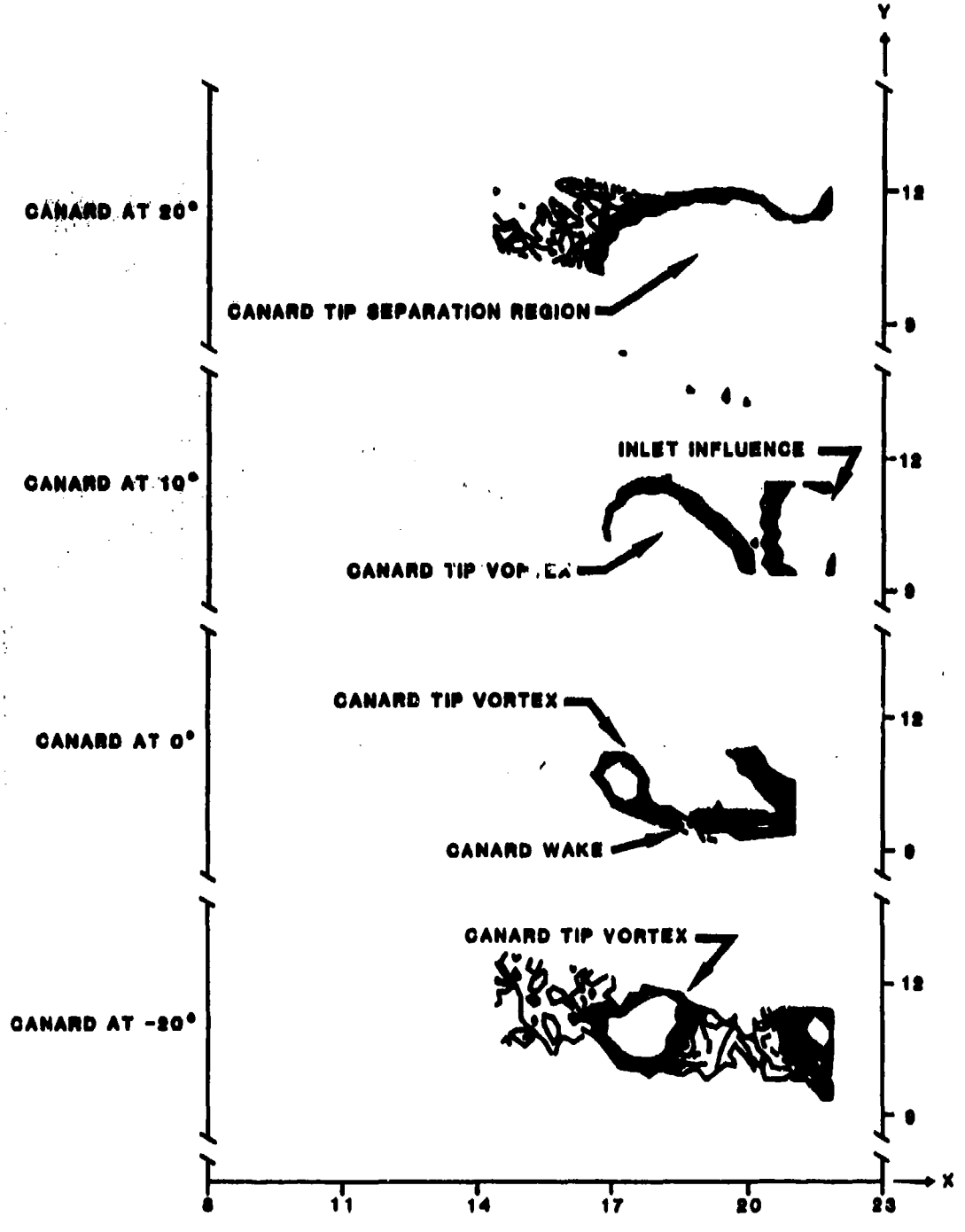

Figure 10. Contours of Constant C_{P_o} for Data Plane 1

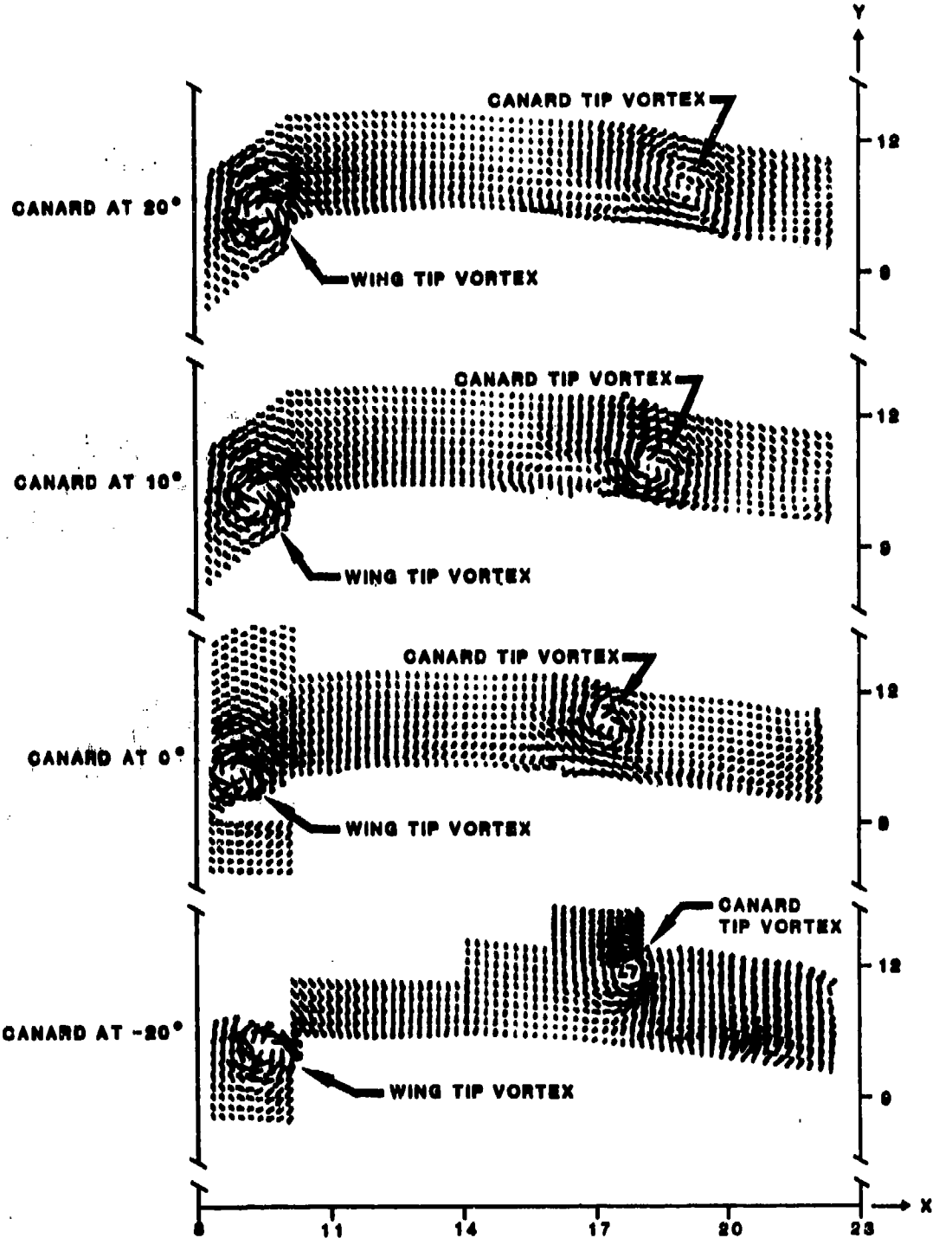

Figure 11. Velocity Vectors for Data Plane 2

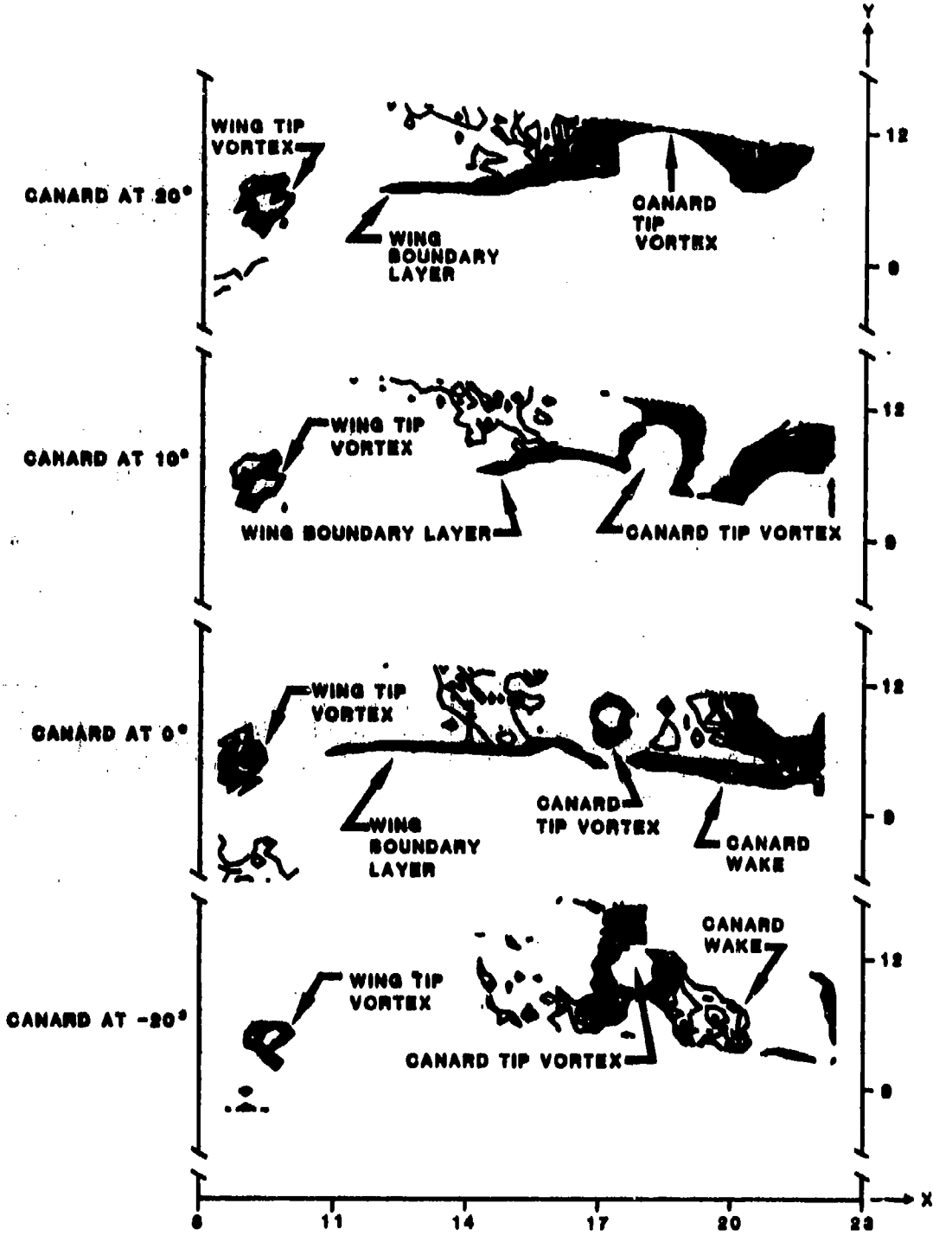

Figure 12. Contours of Constant C_{P_o} for Data Plane 2

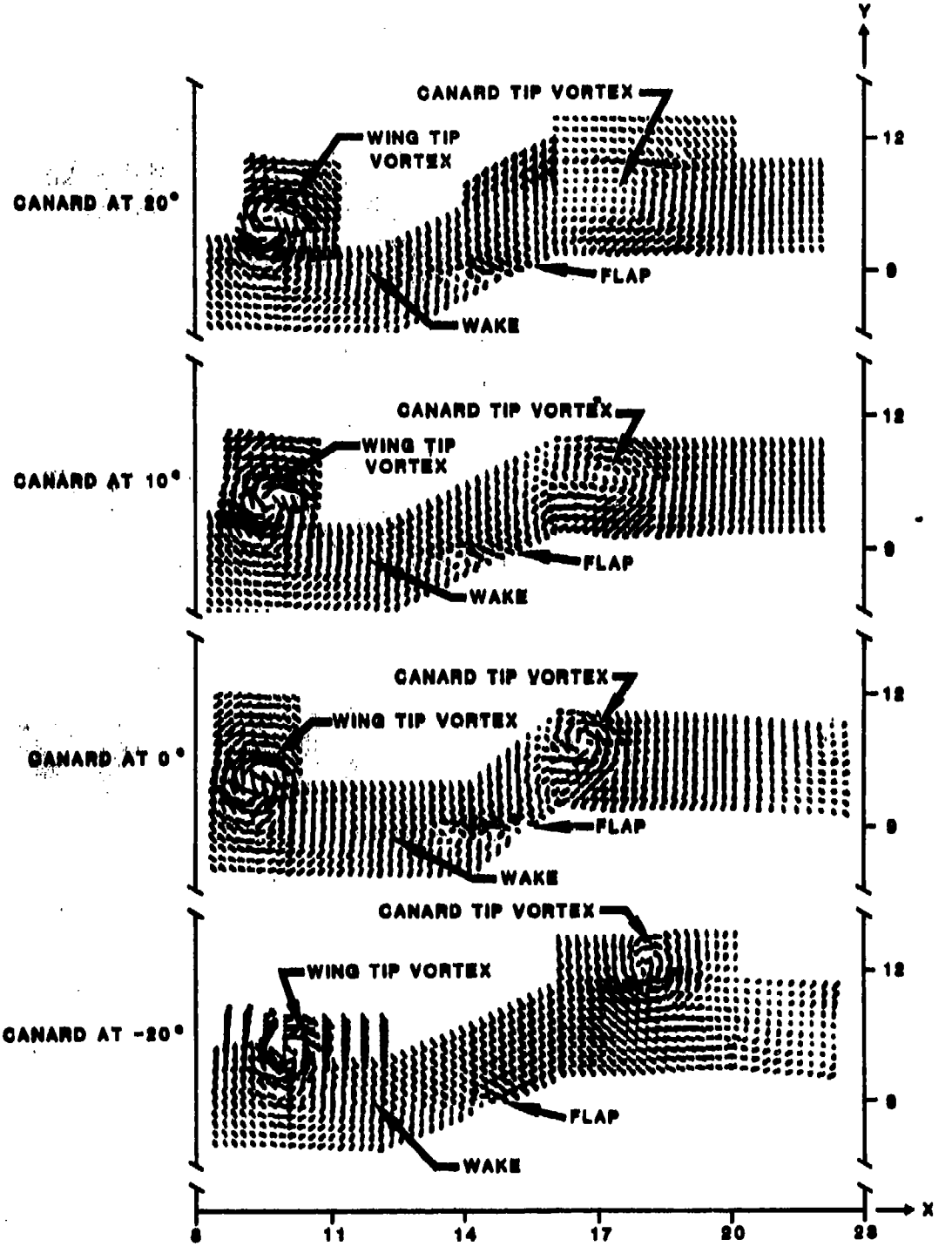

Figure 13. Velocity Vectors for Data Plane 3

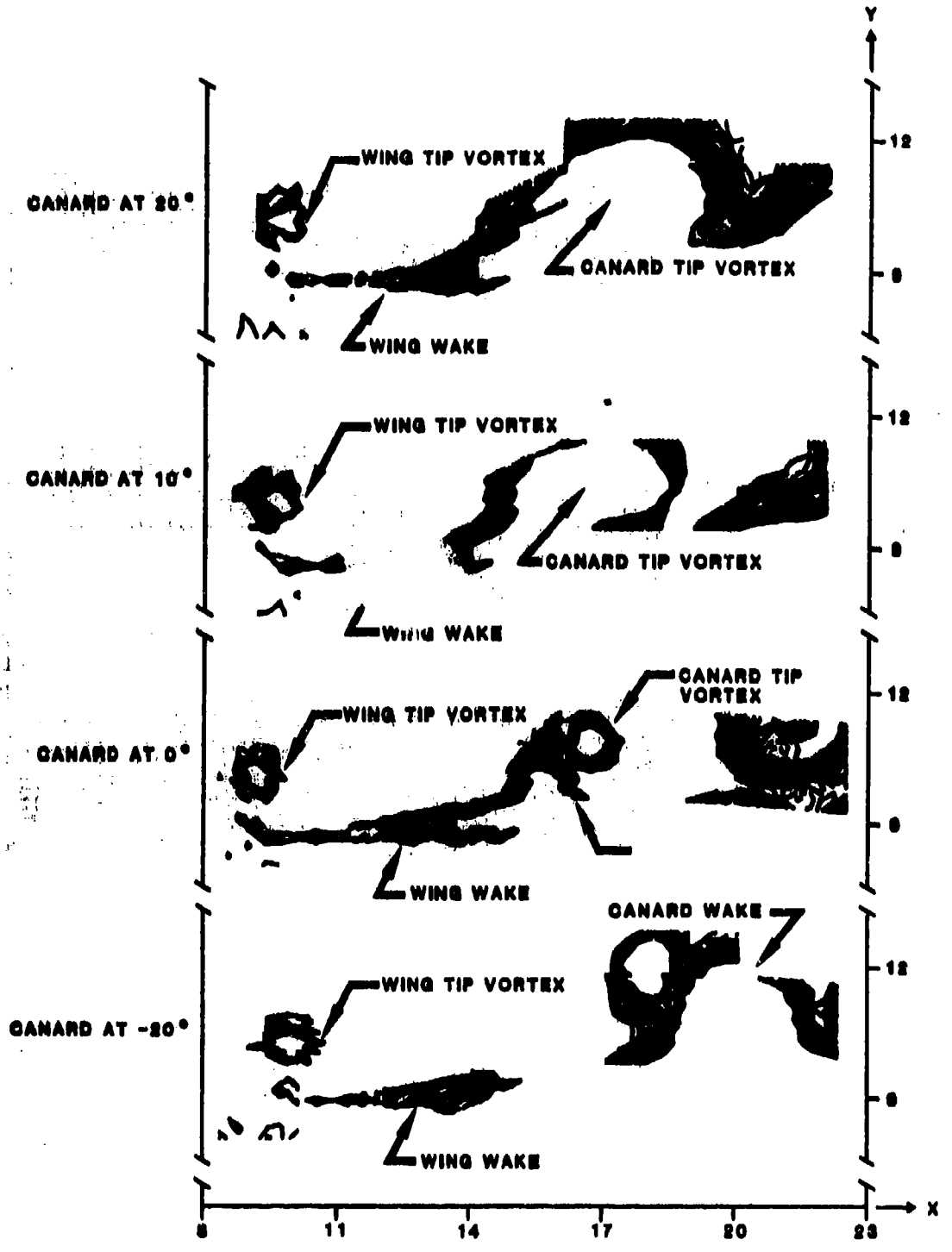

Figure 14. Contours of Constant C_{P_o} for Data Plane 3

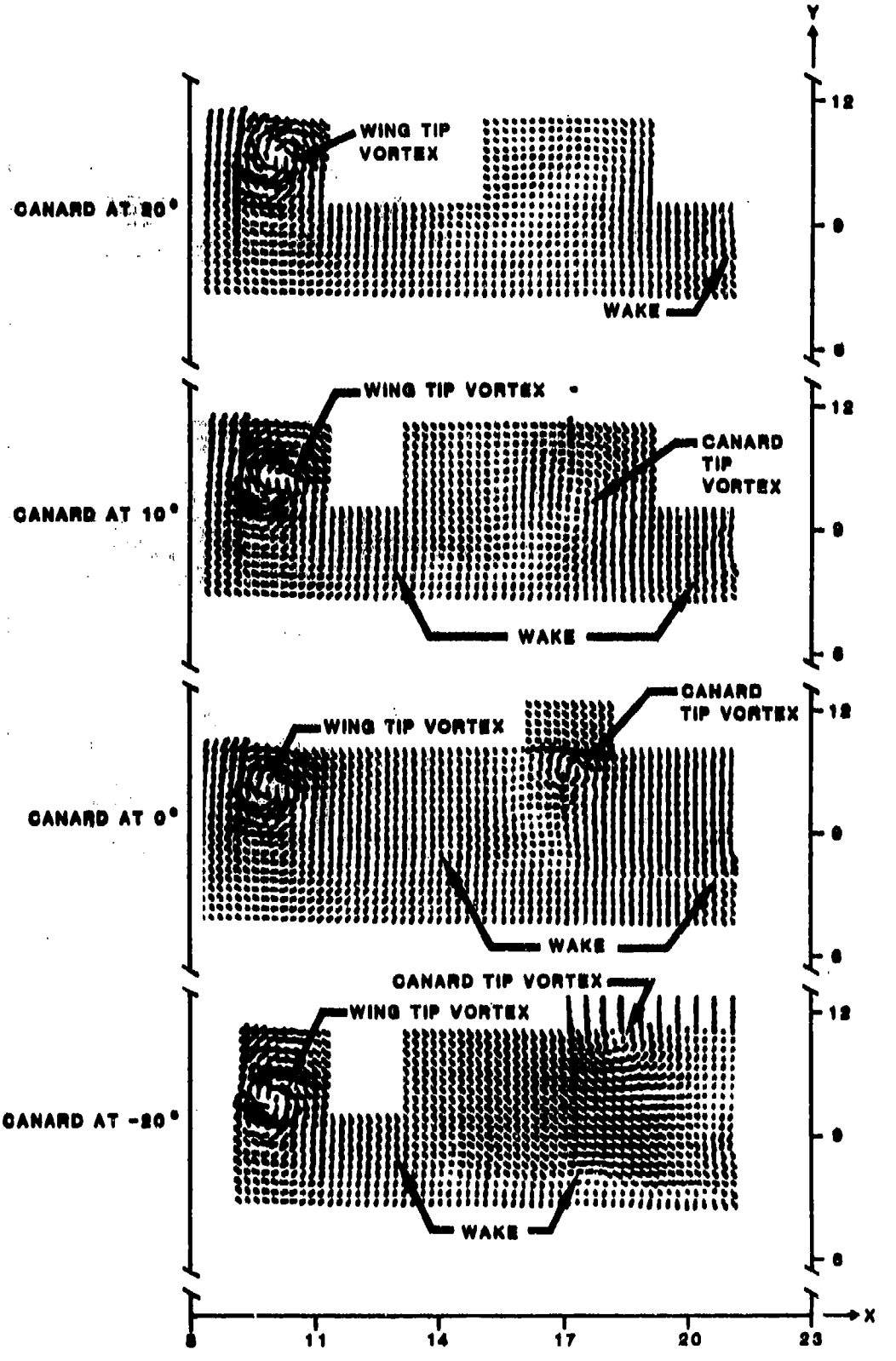

Figure 15. Velocity Vectors for Data Plane 4

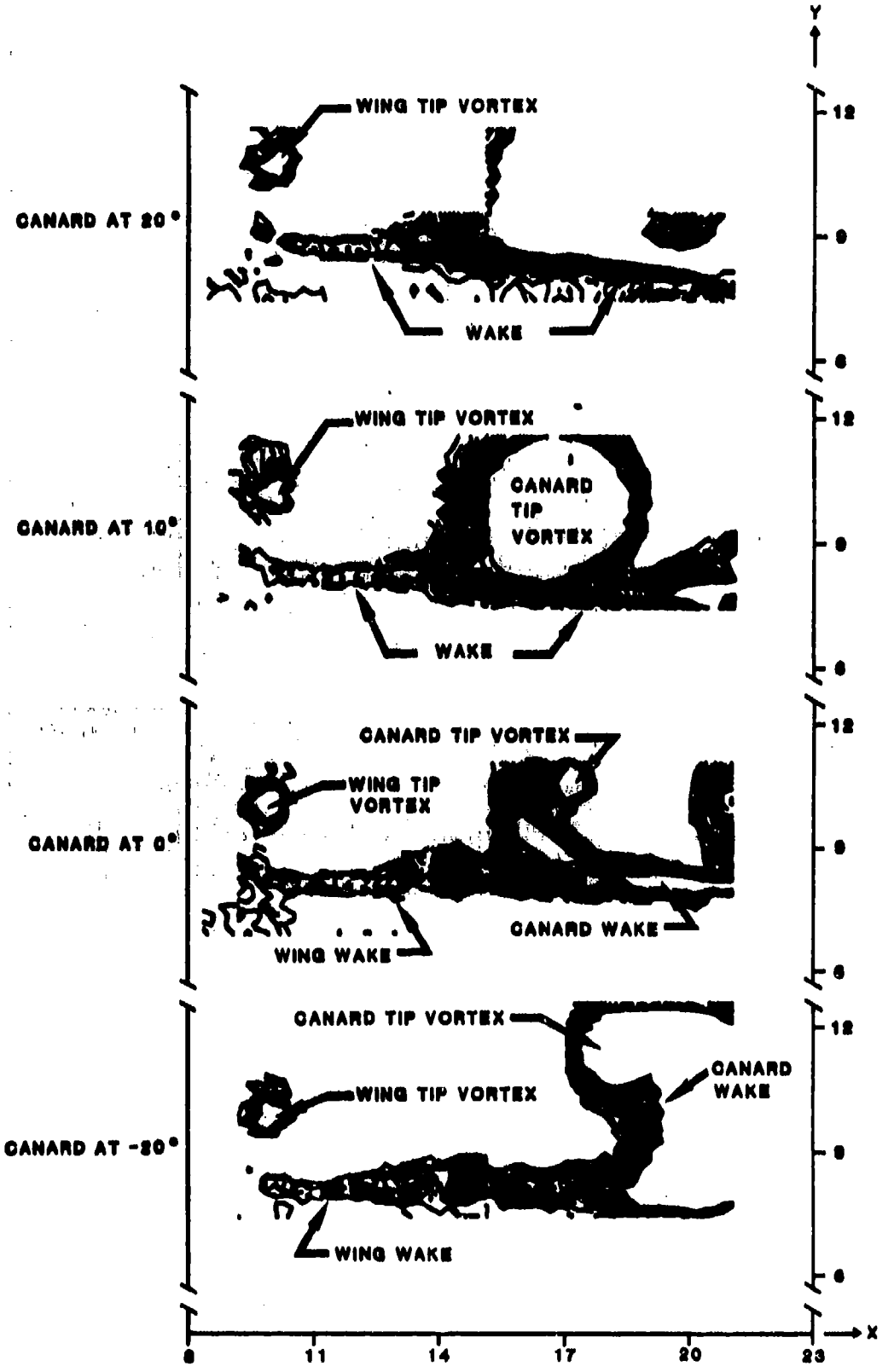

Figure 16. Contours of Constant C_{p_o} for Data Plane 4

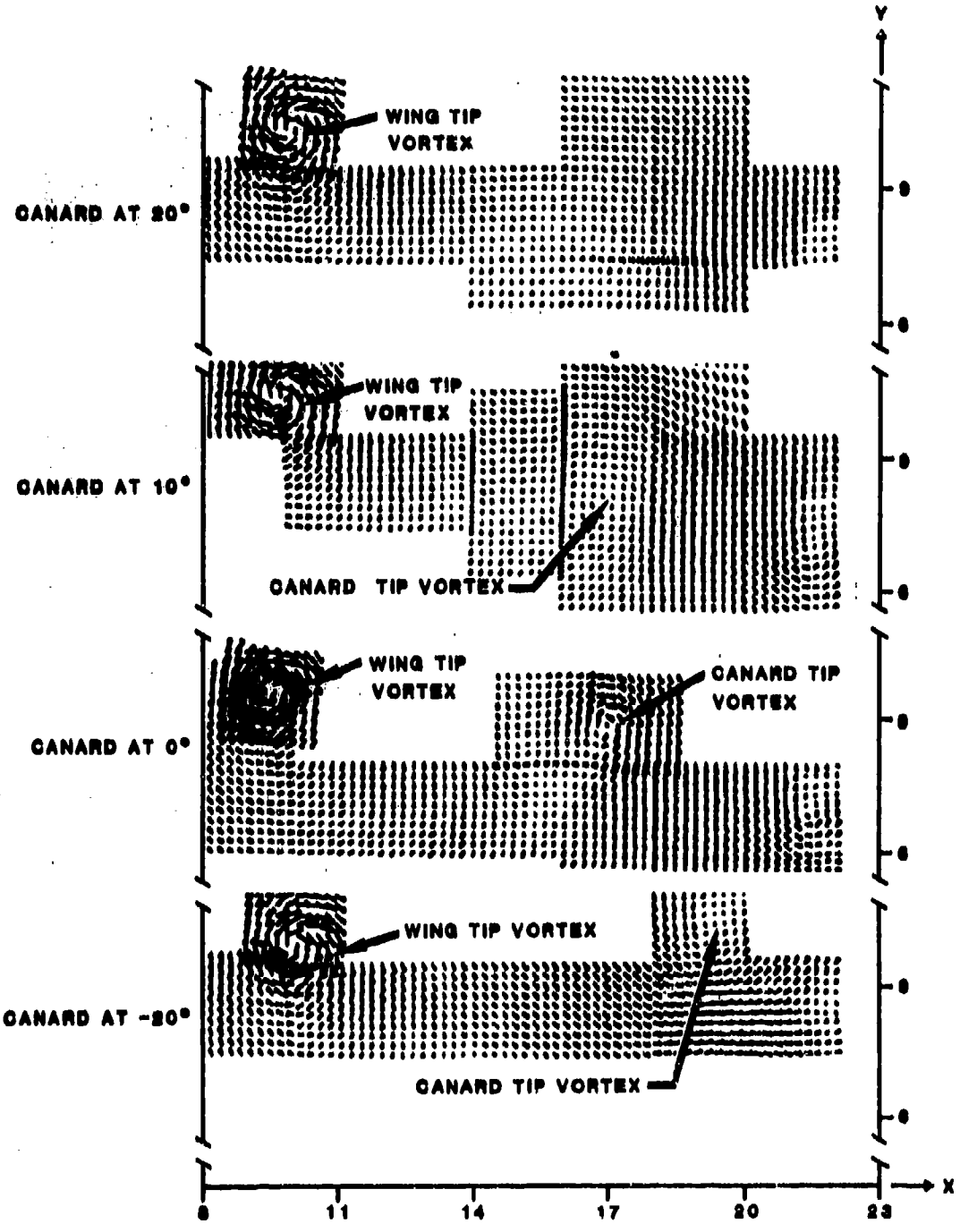

Figure 17. Velocity Vectors for Data Plane 5

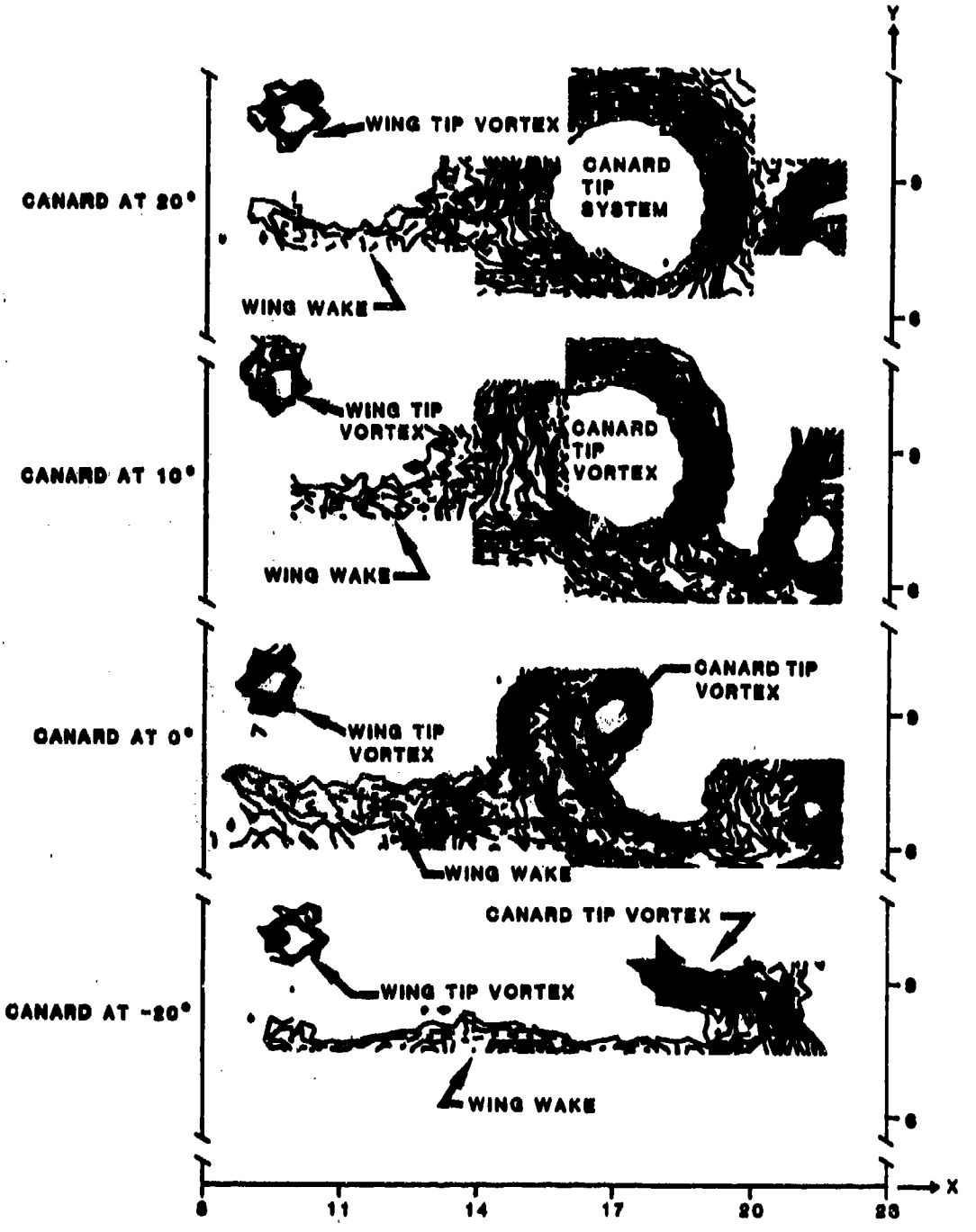

Figure 18. Contours of Constant C_{P_o} for Data Plane 5